

Electrochemical Study of Prussian White Cathodes with Glymes – Pathway to Graphite-Based Sodium-Ion Battery Full Cells

Sai Gourang Patnaik,*^[a, c] Ines Escher,^[a] Guillermo A. Ferrero,^[a] and Philipp Adelhelm*^[a, b]

Prussian white (PW) cathodes exhibit extremely fast rate kinetics for sodium ion (Na^+) insertion/de-insertion at relatively high potentials. However, one of the major bottlenecks is to pair them with appropriate anode materials having similar rate kinetics. Herein, the combination of graphite anodes and several glyme-based electrolytes as appropriate building blocks for PW cathodes to achieve high power density without compromising on energy density is reported. Low defect, Na-rich PW is synthesized, and its electrochemical behavior is

studied with conventional carbonate-based electrolytes as well as with diglyme (2G), tetraglyme (4G) and a 1:1 mixture of 2G and 4G. The stability of the electrolytes is also monitored via *in situ* (*operando*) pressure cell measurements. Graphite | electrolyte | PW cells are then studied in both two and three electrode configurations. It was found that glymes are compatible with the graphite/PW electrode pair and the resulting cells exhibit very good cyclability and rate capability.

Introduction

Sodium-ion batteries (SIBs) are widely viewed as a more sustainable counterpart to current day lithium-ion batteries (LIBs) but are yet to catch up in terms of their energy and power density. High performance and environmentally benign materials in electrodes, coupled with safe electrolytes are thus need of the hour for SIB technology to evolve as a game changer. In this pursuit, Prussian blue (PB) and its analogues (PBAs) have emerged as a feasible technology with commercial promise, evinced by successful large and small industrial enterprises like CATL, Natron energy, and Altris. PBAs are coordination polymers consisting of metal hexacyanometallates having the general formula, $\text{A}_x\text{T}[\text{M}(\text{CN})_6]_y \cdot \square_{1-y} \cdot z\text{H}_2\text{O}$ where A is the mobile cations (Li^+ , Na^+ , K^+); M is the carbon-coordinated transition metal ion (Fe, Mn, Cr); T is the nitrogen-coordinated transition metal ion (can be changed by utilizing appropriate

precursors); \square is $[\text{M}(\text{CN})_6]$ vacancies occupied by coordinating water; $0 \leq x \leq 2$; $0 \leq y < 1$.^[1-3] The hexacyanoferrate based Na rich Fe analogue, represented as $\text{Na}_x\text{Fe}[\text{Fe}(\text{CN})_6] \cdot \square_{1-y} \cdot z\text{H}_2\text{O}$ or commonly termed as Prussian white (PW) is a case in point with the vacancy free congener, i.e., $\text{Na}_2\text{Fe}[\text{Fe}(\text{CN})_6]$ possessing a theoretical capacity of 171 mAh g⁻¹. Their open framework structure has pore size perfectly matching Na^+ ,^[4] as a result, they exhibit very less volume expansion during reversible Na^+ storage. Compared to Na^+ σ-bonding with O 2p orbitals in metal oxide-based cathodes, the relatively weaker Na^+ interaction with C≡N⁻ allows for high-rate capability and facilitated diffusion through the PBA matrix during intercalation/deintercalation. For instance, Wang et al. observed only ~4% volume expansion with rhombohedral $\text{Na}_{2-x}\text{Fe}[\text{Fe}(\text{CN})_6]$ during a single charge-discharge cycle.^[5] Moritomo et al.^[4] reported a cation diffusion coefficient (D) of $0.9 \times 10^{-9} \text{ cm}^2 \text{s}^{-1}$ for $\text{Na}_{0.68}\text{Ni}[\text{Fe}(\text{CN})_6]_{0.675} \cdot 5.0\text{H}_2\text{O}$ and Pasta et al.^[6] reported D values in the range of $10^{-7} \text{ cm}^2 \text{s}^{-1}$ for $\text{Na}_{1.05}\text{Mn}[\text{Fe}(\text{CN})_6]_{0.79} \cdot 1.88\text{H}_2\text{O}$. They are also electrochemically active within the stability window of the commonly utilized carbonate-based organic electrolytes and have been studied extensively in both half (Na metal as anode) as well as full cell (anodes other than Na metal) configurations.

However, there have only been limited reports on the electrochemical behavior of PW cathodes in conjugation with glyme (linear ethers) based electrolytes. Glymes have been extensively utilized in metal-air and metal-sulfur battery chemistries.^[7,8] The wide liquid range, low volatility, and relative stability towards reduced O₂ species of certain ethers like diethylene glycol dimethyl ether (2G), tetra ethylene glycol dimethyl ether (4G) make them well suited for application in Li–O₂ and Na–O₂ batteries.^[9] Similarly, compared to cyclic esters, ethers are more stable towards sulfur and are not susceptible towards nucleophilic attack from polysulfides, hence are also favorable for lithium-sulfur and sodium-sulfur

[a] Dr. S. Gourang Patnaik, I. Escher, Dr. G. A. Ferrero, Prof. P. Adelhelm

Institut für Chemie
Humboldt Universität zu Berlin
Brook-Taylor-Str. 2, 12489 Berlin, Germany
E-mail:
E-mail: Sai.Gourang.Patnaik@imec.be
philipp.adelhelm@hu-berlin.de

[b] Prof. P. Adelhelm
Joint Research Group Operando Battery Analysis
Helmholtz-Zentrum Berlin
Hahn-Meitner-Platz 1, 14109 Berlin, Germany

[c] Dr. S. Gourang Patnaik
Current affiliation:
Energy storage and conversion team (ESC)
IMEC, B-3001Leuven, Belgium

 Supporting information for this article is available on the WWW under
<https://doi.org/10.1002/batt.202200043>

 © 2022 The Authors. Batteries & Supercaps published by Wiley-VCH GmbH.
This is an open access article under the terms of the Creative Commons Attribution License, which permits use, distribution and reproduction in any medium, provided the original work is properly cited.

battery chemistries.^[10,11] More recently, glymes have received renewed research interest owing to their ability to coordinate to active alkali metal ions, thus enabling a reversible solvent co-intercalation behavior with Na^+ in graphite^[12–16] forming ternary graphite intercalation compounds (*t*-GIC). This behavior is interesting, as graphite is largely inactive for Na storage in cells with conventional carbonate-based electrolytes as binary Na-GICs are energetically unfavorable.^[17] Moreover, glymes also exhibit very high first cycle Coulomb efficiency (ICE) with graphite^[15] due to a probable “SEI free” interface,^[18,19] compared to hard carbon anodes utilizing carbonates for Na^+ cycling, and hence are advantageous for fabrication of full cells. The large volume change during cycling may be mitigated by choosing different binders or adding additional co-solvents.^[20] In the cathode side, the high voltage anodic instability of glymes is debatable, but there have been many reports on successful utilization of glymes in conjugation with high voltage cathodes for both Li and Na ion chemistries.^[21–23] In a related context, the open framework PW cathodes can also be expected to accommodate solvent coordinated Na^+ ions and hence provide an interesting stage for solvent dependent electrochemical properties as exhibited by graphite. This will also bring forth the idea of utilizing graphite as a mainstream anode option for SIBs, which has been primarily dominated by hard carbon, alloys/metals, or chalcogenides.^[24] In addition, the high-rate capability of graphite anodes with glymes will also complement the existing research efforts to find appropriate high-rate capability anodes for PBA based cathodes.

In this pursuit, we examined the electrochemical behavior of Na-rich PW cathodes in various cell configurations using different electrolytes (carbonates as well as glymes). We first study and draw comparison between performance of PW cathodes with carbonates and glymes in their half-cell configuration with Na metal. Taking advantage of high ICE of both graphite and PW electrodes, stepwise fabrication of full cells in both three electrodes (W.E.: PW cathode, R.E.: Na metal, C.E.: graphite anode) as well as two electrode configurations is then demonstrated with high-rate capability and long-life cycle. The advantage of utilizing two high-rate capability electrodes in compatible solvent systems is then clearly exhibited by decoupling of the inverse relationship of energy/power density in the final full cells (between 0.1 and 1 A g^{-1}).

Results and Discussions

Synthesis of Prussian white

Fully reduced and sodiated form of PB (also known as PW) are advantageous owing to their applicability in full cells without the need for reactive sodium loaded anodes as reservoirs for the active ion. Perfectly sodiated PW would also lead to a vacancy free framework and ensures preservation of the intercalation sites for Na^+ during the high temperature vacuum drying process required to obtain moisture free PW particles. Single precursor synthesis originally reported by Guo et al.^[25] achieved vacancy free PB albeit with very low sodium content

because of Fe^{2+} oxidation. Brant et al.^[26] later reported a systematic study on the evolution of structural properties of PW cathodes with modification to the synthetic procedure to include increased sodium content and obtained an initial charge capacity of 158 mAh g^{-1} by suppressing Fe^{2+} oxidation through constant N_2 purging during synthesis. More recently, Tan et al.^[27] synthesized PW in a two-step mild and low temperature process, where they first synthesized PB and then reduced it with NaBH_4 to achieve PW with near theoretical capacity of ~169 mAh g^{-1} . For the current work, we adopted the single precursor PW synthesis by Brant et al. with certain modifications. Notably, we increased the reaction time to 48 h under constant Argon purging in 1 M NaCl solution. The extended time was chosen to grow micrometer sized particles whereas constant Ar purging was done to prevent Fe^{2+} oxidation. The introduction of NaCl in the reaction mixture was to increase the amount of Na^+ in the final PW framework.^[28] The color of the reaction flask at the end of the reaction was still white (suggesting presence of large amount of intercalated Na^+)^[29] with slight blueish tinge and turned light blue after work up (Figures 1a and S1, perhaps because of loss of some of the sodium ions due to presence of surface water). The ratio of Na/Fe (=0.648) was determined by Inductively coupled plasma atomic emission spectroscopy (ICP-OES) measurements. Scanning electron microscope (SEM) images (Figures 1b and S2) show micrometer-sized homogenous particle distribution. The XRD pattern of the dried PW (120 °C, 12 h, Figure 1c) exhibited a monoclinic (P21/n) phase with high crystallinity. The Raman spectra (Figure 1d) of the dried PW showed two clear $\nu(\text{CN})$ stretching modes at 2130 and 2094 cm^{-1} , respectively with a small shoulder at 2111 cm^{-1} , which can be assigned to A_{1g} , E_g and T_{1u} vibrations owing to the local O_h group symmetry with an inversion center as reported earlier.^[30,31] The IR spectrum of PW (Figure 1e) exhibited two narrow bands at 3547 and 3613 cm^{-1} which correspond to symmetric and asymmetric O–H stretching vibrations and an H–O–H bending vibration at 1614 cm^{-1} which can be either because of crystal or surface water. The average valence state of Fe can alter the prominent $\nu(\text{CN})$ band at 2072 cm^{-1} leading to peak splitting in case of different chemical environment around Fe^{3+} .^[32] Appearance of a single prominent peak in case of PW thus indicates a uniform chemical environment around Fe in case of PW. The narrow peaks between 3500–3650 cm^{-1} compared to broad peaks for the starting precursor indicate a low water content. This was also confirmed from thermo gravimetric analysis (TGA) (Figure 1f). In case of PW, water can exist either adsorbed on the surface, or as coordinating water in the framework (in place of $[\text{Fe}(\text{CN})_6]^{4-}$ vacancies to maintain the cubic lattice).^[33] Majority of the surface adsorbed water content can be removed by vacuum drying. Hence, negligible amount of remaining adsorbed water is released at ~100 °C and most of the crystal water is released between 150–240 °C and leads to cracking of the particles as reported earlier.^[32] Further heating >400 °C leads to stepwise decomposition of the entire framework.

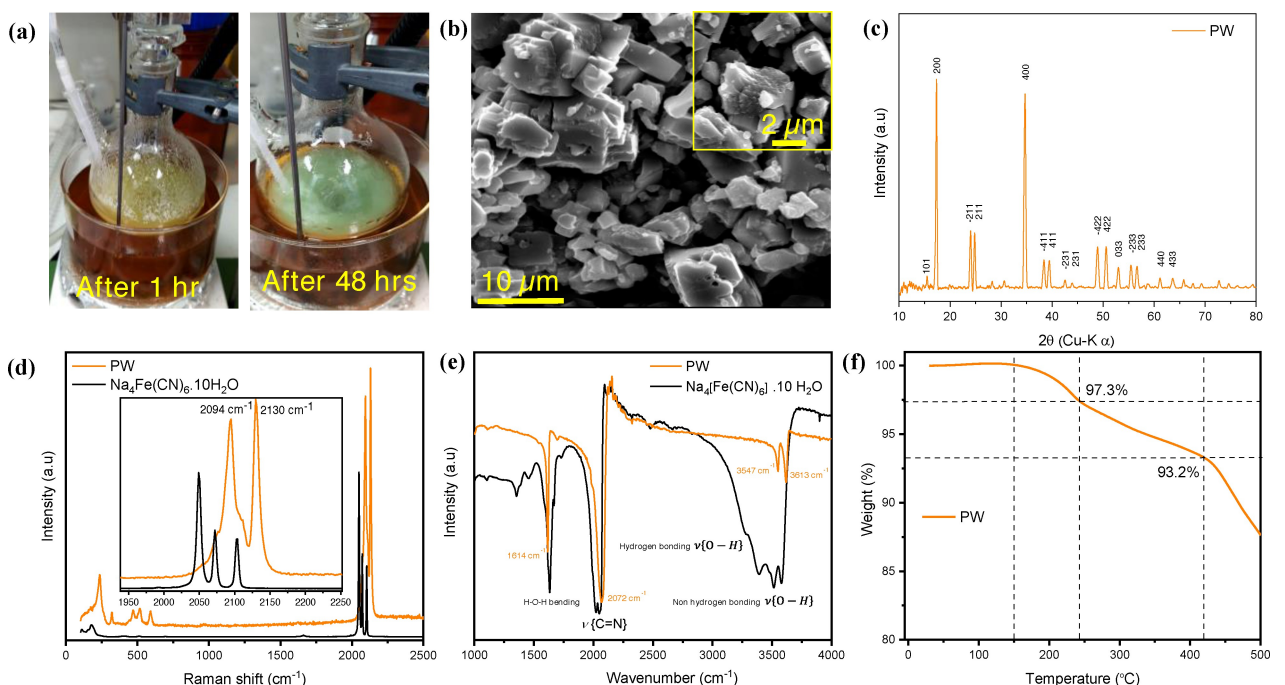


Figure 1. Characterization of dried PW: a) Digital images of the reaction mixture in the beginning and upon completion of reaction, b) SEM images at different magnifications, c) XRD pattern after drying. d) Comparison of Raman spectra with starting precursor. e) Comparison of IR spectra with starting precursor. f) TGA curve (under N₂ atmosphere, at a ramp rate of 5 °C min⁻¹).

Electrochemical studies with sodium-metal anode

Electrodes were fabricated with PVDF as binder and Super P as carbon additive. NaPF₆ was adopted as the salt of choice. These were obtained from reports from previous optimizations with PB analogues.^[34] The behavior of the PW electrodes was first evaluated in different conventional carbonate-based electrolytes and with diethylene glycol dimethyl ether (2G), tetraethylene glycol dimethyl ether (4G) and a 1:1 mixture of 2G/4G in two electrode half-cell set up with Na metal as the counter electrode. The sodium rich nature of PW was conspicuous during the first

de-sodiation cycle in different electrolytes with an average of ~145 mAhg⁻¹ capacity correlating to high initial sodium content (~1.7 Na per formula unit) in the synthesized PW (Figure 2a). The galvanostatic charge-discharge profiles showed two-step charging with plateaus at 3.1 V and 3.3 V vs. Na⁺/Na respectively and contributing almost equal capacity (Figure 2b). A similar two step trend was also observed during the discharging step. The discharge plateaus for the high voltage charging counterpart were also at similar potential of ~3.3 V vs. Na⁺/Na but the low potential plateau showed some variation. The trend for this low potential plateau was in the order 4G~2G (~3.02 V vs. Na⁺/

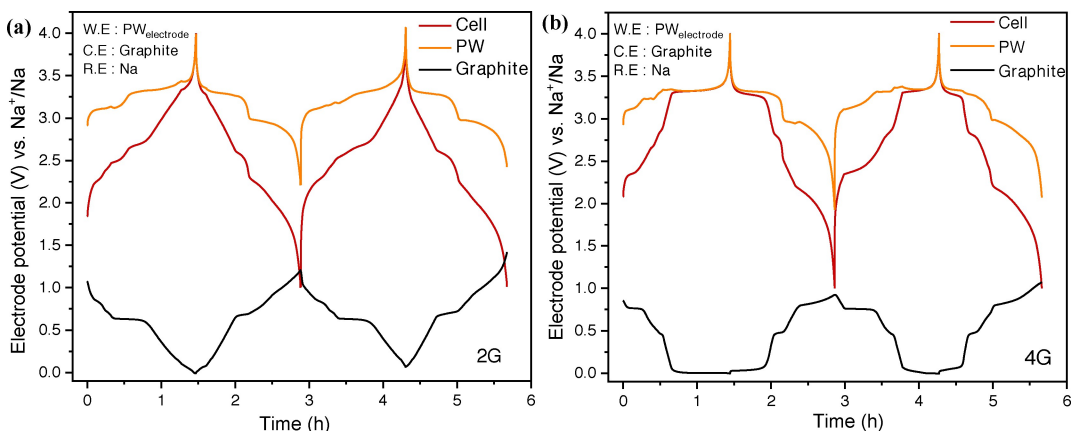


Figure 2. Electrochemical characterization in different electrolytes: a) comparison of first charging cycle showing high Na content of the PW electrodes at 0.025 A g^{-1} , b) comparison of galvanostatic charge/discharge profiles at 0.025 A g^{-1} (2nd cycle), c) comparison of capacity retention at different charging rates, d) comparison of capacity retention during cycling at 1 A g^{-1} .

$\text{Na}^+ > 2\text{G}/4\text{G} > \text{EC/PC/FEC}$ (~ 2.99 V vs. Na^+/Na) $> \text{EC/PC}$ (~ 2.94 V vs. Na^+/Na). An explanation why this behavior is only found during sodiation is not straightforward, however, it may relate to differences in solvation/desolvation kinetics of Na^+ ions in the different solvents. It seems not specifically related to differences in the cathode electrolyte interface, as no such trend was observed during de-sodiation. The rate capacity retention at increasing current densities showed a trend in the order $2\text{G} > 4\text{G} > 2\text{G}/4\text{G} > \text{EC/PC/FEC} > \text{EC/PC}$. This trend can be understood by considering studies reported by Vitoriano et al.^[35] The superior rate performance of 2G (ionic conductivity, $\sigma = 5.64 \text{ mS cm}^{-1}$ and viscosity $\eta = 2.42 \text{ mPas}$ at 25°C for 1 mol dm^{-3} concentration of NaPF_6)^[21] compared to 4G (viscosity $\eta = 3.39 \text{ mPas}$ at 25°C)^[36] can be ascribed to its higher ionic conductivity (lower viscosity) and higher de-solvation ability (low chelating strength compared to 4G). The mixture of $2\text{G}/4\text{G}$ doesn't lead to any enhancement in rate performance compared to the individual solvents in this cell configuration but is still superior to carbonate-based electrolytes (ionic conductivity, $\sigma = 11.5 \text{ mS cm}^{-1}$ and viscosity $\eta = 2.78 \text{ mPas}$ at 25°C for 1 mol dm^{-3} concentration of NaPF_6 in 1:1 EC/DMC).^[21] Long cycling studies, however, show better stability with 4G (as a deviation from the trend of rate studies) than 2G and the rest showing the same trend as that of rate studies. This can be because highly chelating 4G shields Na^+ ion from possible side reactions with moisture content (inevitably present in small quantities in PW cathodes) which has been reported as predominant mode of failure for these class of cathodes.^[37] The overall results thus indicate better stability of the glymes for PW electrodes compared to carbonates with Na metal anodes. To further evaluate the compatibility of the PW electrodes with the solvents

and probability of gas evolution, we performed pressure evolution measurements (Figures S3 and S4). As electrolyte decomposition leads to gas release, this method can provide clear hints for side reactions. This is especially important as glymes are generally considered to have a limited stability at high potentials. From our experience, electrolyte decomposition can lead to pressure variation of $\sim 1\%$ per cycle. The pressure changes for all electrolytes were, however, much smaller than this value. Even over 5 cycles, the relative pressure variation was within a $\pm 1\%$ corridor, a change that is likely only due to signal drift of the setup. Overall, no signs for electrolyte decomposition were detected (within the detection limits of the pressure cell), indicating cycling of the PW cathodes occurs without side reactions in both ether and carbonate electrolytes.

Full cell studies with graphite anode

One of the major advantages of glymes for SIBs is their applicability to graphite anodes due to solvent co-intercalation phenomenon. Figure S5 shows the first charge/discharge profiles of graphite | Na-metal cells with various glymes used previously for Na | PW cells. Hence it was imperative to examine PW cathodes in conjugation with graphite anodes while studying gylme-based electrolytes. To get better understanding of the potential window of operation, three electrode measurements were conducted (Figure 3). The cell voltage was controlled between 1.0 – 4.0 V and the electrode potentials were monitored with respect to the Na reference during constant current operation. In case of 2G (Figure 3a), the potential of the counter electrode never encroached negative potentials where-

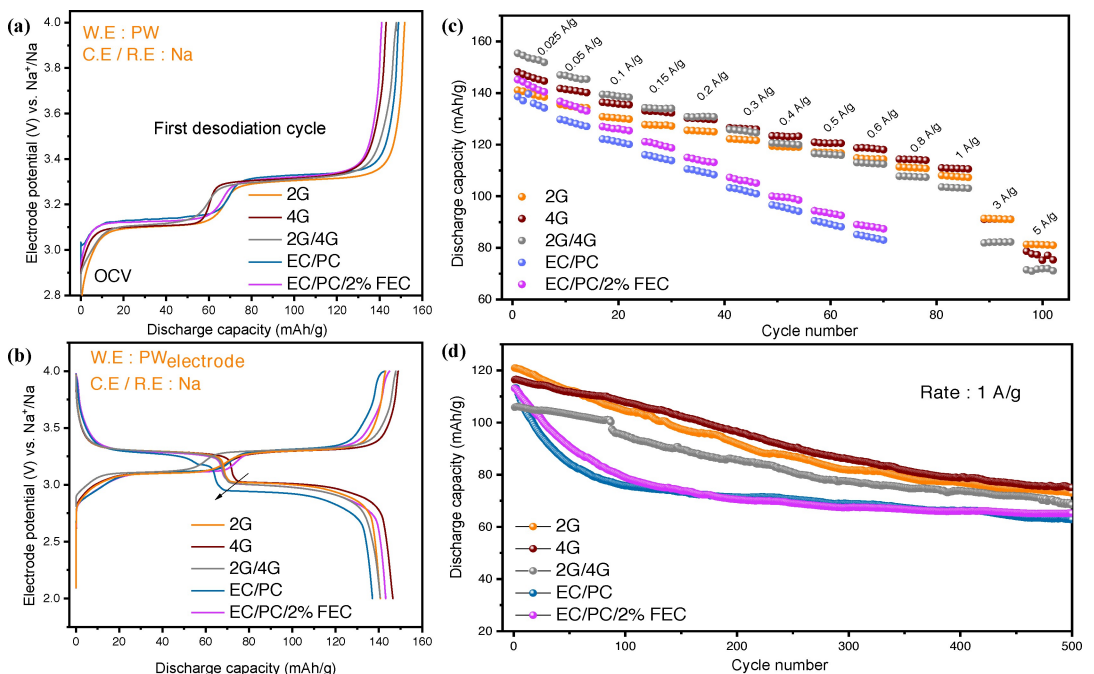
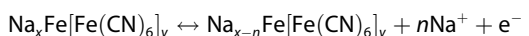


Figure 3. Electrochemical characterization in three-electrode set-up, potential time profile during galvanostatic cycling at 0.1 A g^{-1} for: a) 2G (anode/cathode capacity = 1.18 mAh), b) 4G (anode/cathode capacity = 1.33 mAh).

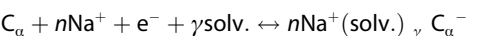
as in the case of 4G (Figure 3b), the counter electrode potential reached -0.005 V vs. Na^+/Na , indicating possibility of Na plating. It is important to note here that the potentials monitored by the potentiostat are an average of the entire porous electrode, and do not provide a clear picture of localized potential distributions and electrochemical processes occurring thereof. In case of 4G (Figure 3b), the cell voltage (E_{cell}) coincided with the high voltage plateau of PW during the first sodiation cycle and an extended reversible low potential plateau was observed for graphite sodiation (because of some amount of Na plating as mentioned before). However, this plateau decreased during the subsequent cycles and was also not observed during studies in two electrode configurations. In case of 2G (Figure 3a), no such extended plateau was observed and E_{cell} exhibited a sloping profile without coinciding with W.E. contrary to that of 4G (in the de-sodiation cycle). This gives an impression about the relatively labile nature of 4G electrolyte with respect to Na metal compared to 2G.

After establishing the stable voltage window, coin cells with PW cathode and graphite anodes were constructed. The individual electrodes and overall cell reaction can be represented as follows:

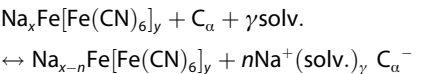
Positive electrode:



Negative electrode:



Overall cell reaction:



where Na^+ ions intercalate together with the solvent molecules (solv.) into the graphite lattice (C_a).

The galvanostatic cycling profiles for all the electrolytes exhibited two steps charging and discharging profile like that of $\text{Na} | \text{PW}$ cells (Figure 4a). The discharge capacity obtained was like that of half cells with sodium as C.E. at the given current rate, thus showcasing good electrode/electrolyte compatibility in this configuration. A comparison of the anodic and cathodic half cells with full cells is provided for better reference in the supporting section (Figures S6–S8). The potential positioning of the lower discharge plateau (sodiation) onset at ~ 2.5 V followed the same trend as that of half-cells as $4\text{G} \sim 2\text{G} > 2\text{G}/4\text{G}$. The trend in rate capacity retention too matched that of $\text{Na} | \text{PW}$ cells as $2\text{G} > 4\text{G} > 2\text{G}/4\text{G}$, with 2G having highest capacity retention upon increasing current density (Figure 4b). This indicates that the rate behavior is determined by the PW cathode. The charge/discharge profiles at different rates for the electrolytes in full cell configuration

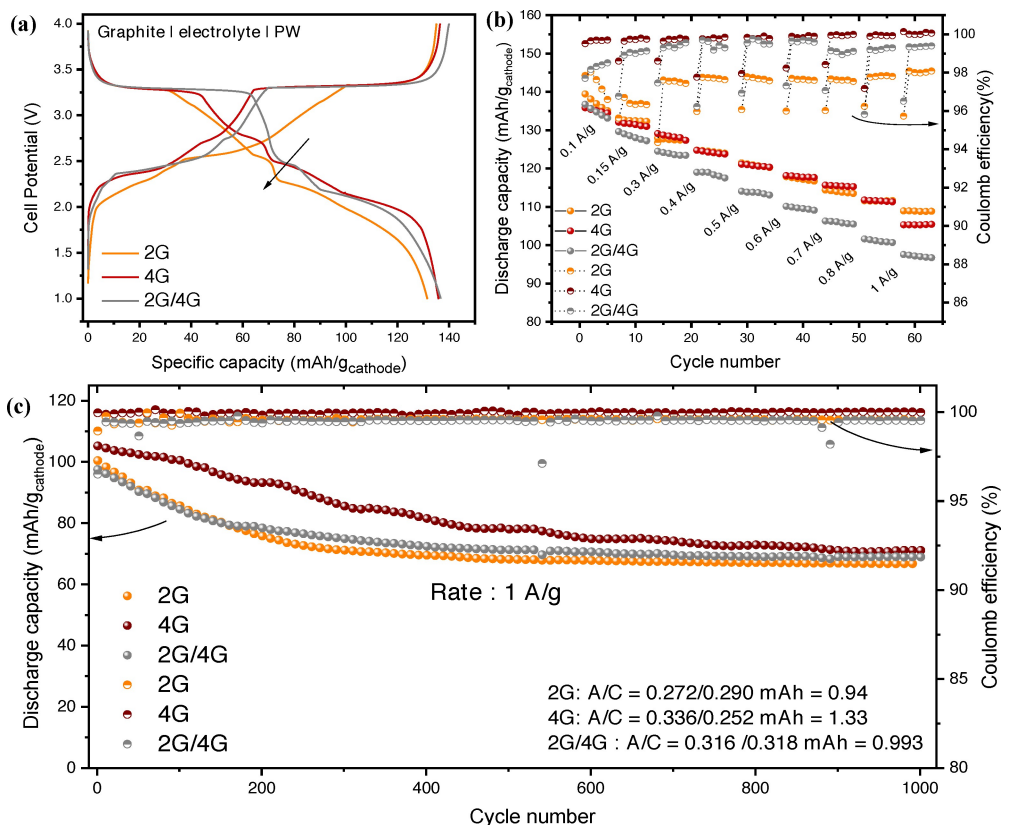


Figure 4. Electrochemical characterization of graphite | PW full cells: a) comparison of galvanostatic cycling at 0.1 A g^{-1} , b) comparison of capacity retention at increasing charging rates for different electrolytes.

show interesting features (Figure S9). Two distinct plateaus can be observed for 2G (Figure S9a) but the plateau at higher potential exhibits much less current dependency compared to the one at lower potential. The profiles for 4G (Figure S9b) and 2G/4G (Figure S9c) showed the expected two step profiles having equal contributions even at higher rates. The magnitude of capacity drop though was slightly higher for graphite | PW as compared to Na | PW cells, mostly because of limited availability of sodium in the former case. The graphite | PW cells were very stable towards cycling with >94% capacity retained after 1000 cycles at a high current density of 1 A g^{-1} . This is contrary to Na | PW cells, where 40% capacity drop was observed in most electrolytes just after 500 cycles at the same current, which can be explained by the reactivity of organic electrolytes with Na metal reported previously.^[31,39,40] The shift in Coulomb efficiency was in the order 4G > 2G > 2G/4G, which further strengthens our assumption of shielding the Na^+ ions from water molecules by the highly chelating 4G. To see if there is any possible dissolution of the electrode materials, the cycled cells were opened and do not show any severe signs of electrode degradation (Figure S10). The small dark specs on the anodic side of the separator were further examined with SEM and EDX mapping to trace any possible crossover of Fe ions, but the elemental composition scans clearly confirmed absence of any Fe content in separators for any of the electrolytes utilized for graphite | PW full cells (Figures S11–S16). Nevertheless, it is also important to realize that reports exist that show a much longer cycle life for electrode reactions in half cell geometry. This includes Na | graphite^[41,42] or Na | carbon-tin^[43] which, as anodes, operate at potentials close to Na metal. The more rapid fading of the PW cathode material in half cell geometry requires therefore another factor in addition to the reactivity of Na with the electrolyte, e.g., cross talk between the electrodes including reactions due to the higher redox potential of PW.

We finally compare the performance of our Graphite | PW full cells with different electrolytes in a Ragone plot (Figure 5a).

The energy density reached was $> 157\text{ Wh kg}^{-1}$ and the highest power density achieved was $\sim 553\text{ W kg}^{-1}$ within the measured current rates for the active mass only. At a high charging rate of 1 A g^{-1} both 2G and 2G/4G achieved $> 500\text{ W kg}^{-1}$ while still retaining $> 100\text{ Wh kg}^{-1}$ energy density. More importantly, no drastic decrease in energy density was observed with increase in power density, which is contrary to many other anode/cathode combinations for SIBs. This can be attributed to the choice of the electrodes and electrolytes. Our group has previously reported on high-rate capability of graphite electrodes with glyme based electrolytes towards Na^+ storage based on co-intercalation phenomenon.^[44] In a similar manner, PW based cathodes are also well known for their high-rate capability towards Na^+ owing to their open framework structure and pore size matching. Hence the combination of two such electrodes as anode and cathode with fast Na^+ ion storage kinetics resulted in superlative power density without compromising the energy density within the measured current range. The potential obtained in full cells was $\sim 2.85\text{ V}$ and the highest capacity obtained was $\sim 140\text{ mAh g}^{-1}$ which was on par with other state of art reports (Figure 5b) even though not the highest. The most distinguishing feature, however was the cycling stability of the graphite | PW full cells which was better than most of the other reports in our comparison.^[45–53]

Conclusion

In summary, the compatibility of PW-type cathodes was systematically evaluated with various carbonates and glyme based electrolytes and a comparison was drawn between the two. The compatibility of glymes with graphite anodes was then exploited to construct full cells with energy and power densities up to 157 Wh kg^{-1} and 553 W kg^{-1} respectively and exceptional cycling stability (> 94% discharge capacity retention for over 1000 cycles). Compared to half-cell experiments (with Na metal as counter electrode), the full cells showed a

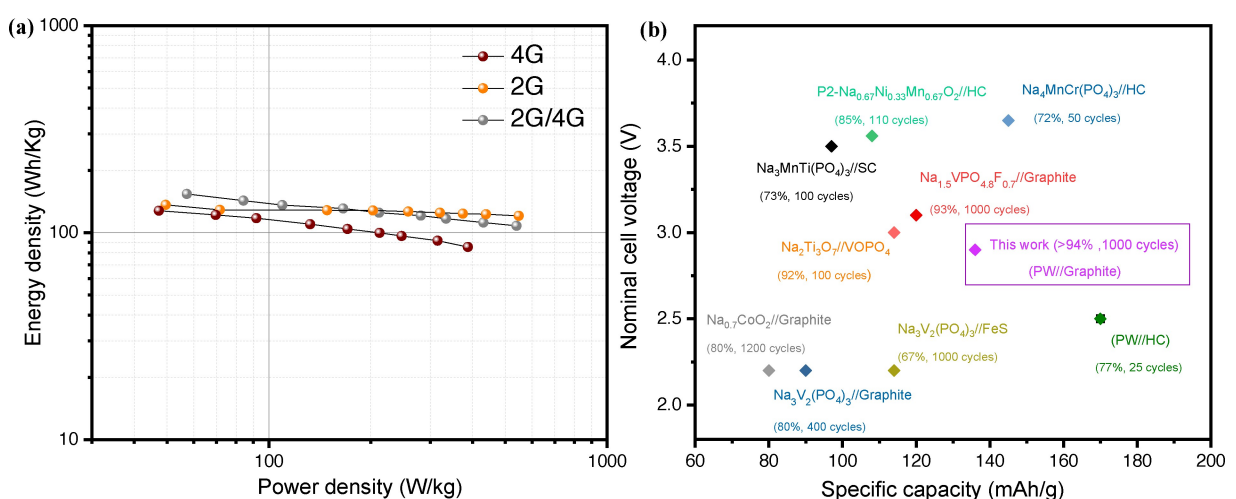


Figure 5. Comparison of PW | graphite full cells: a) in Ragone plot for different electrolytes used (based on active material weight only), b) with other reports (Ref. [26]–[34]) in terms of working potential, cycling stability and cathode capacity.

significantly improved cycle life, indicating that the cycle life of PW cathodes is underestimated in half cells. Since rational matching of anodes, cathodes and electrolytes is crucial for performance enhancement, this is indeed a way forward in utilization of glymes as promising electrolytes for next generation SLBs.

Experimental Section

Synthesis of Fe-PBA

Fe-PBA was synthesized by previously reported single precursor method but with slight modification to maximize the amount of Na as well to maintain the ratio of $\text{Fe}^{3+}/\text{Fe}^+$ in the final product. Briefly, in a typical synthesis, 2 mmol $\text{Na}_4\text{Fe}(\text{CN})_6 \cdot 10\text{H}_2\text{O}$ (Merck) was dissolved in 100 mL of 1 M NaCl solution in deionized water to obtain a homogenous solution. The mixture was maintained at 80°C for 15 min under vigorous stirring and Ar (argon) gas purging followed by dropwise addition of 1 mL of 37% HCl (hydrochloric acid). The solution was then stirred for 48 h under constant Ar purging to obtain PW. The composite was collected by filtration, washed with water several times, and dried at 140°C in a vacuum oven for 12 h.

Material characterization

SEM images were taken with a scanning electron microscope (Phenom Pharos Desktop SEM, Phenom World) using secondary electron detector. XRD measurements were performed with a D2 Phaser instrument from Bruker. A Cu X-ray tube (30 kV, 10 mA) was used to conduct the experiments, using a step width of 0.2°. Elemental analysis was measured using a Euro EA 3000 from EuroVector S.P.A., values shown were the mean values of two measurements. Raman measurements were performed on a Renishaw QONTOR equipment, a transparent CaF_2 cover was used to avoid air exposure. For ICP-OES measurements, known amount of synthesized PW powder was first digested in 3 M HCl solution and ultrasonicated for few hours to achieve a clear solution.

Electrode preparation

The dried Fe-PBA was then finely ground along with dried Super P for at least 30 min with mortar pestle and then added to solution of PVDF (PIKEM Ltd.) in NMP (Sigma Aldrich) and finely mixed using a Thinky mixer. The ratio of components in the composite was Fe-PBA/Super P/PVDF (wt%) (70:20:10) with appropriate amount of NMP (1 ml for 30 mg of Super P) to obtain a thick ink with appropriate consistency. The graphite electrodes contained 90 w/w graphite powder (MTI Corp.) and 10 w/w PVDF as binder material and NMP (Sigma-Aldrich) was used as the solvent to cast electrodes. Electrodes were casted with an initial thickness of 300 μm (for PW) and 100 μm (for graphite), dried overnight under air, punched to the appropriate size (12- or 10-mm diameter), and dried again at 110°C under vacuum overnight. The average mass loading of active material for PW electrodes was $\sim 2.0 \text{ mg cm}^{-2}$ and that of Graphite electrodes was $\sim 2.4 \text{ mg cm}^{-2}$.

Electrochemical measurements

All cell assemblies were performed in an argon-filled glovebox from MBraun. For cells with sodium metal as counter/reference electrode in two electrodes set up, pure sodium (BASF) was rolled

up and punched into disks of equal diameter as that of the working electrode (12 mm diameter) and a glass fibre (GF) separator (Whatman) of 16 mm diameter was used to separate the electrodes. For three electrodes set up, Swagelok type cell was utilised where a small disc of pure sodium metal served as the reference electrode. 1 M solution of NaPF_6 (purity >99%, Alfa Aesar) dissolved in different solvents 2G, 4G, EC/PC (Sigma-Aldrich, pre-dried using activated 4 Å molecular sieves) was used as the electrolyte. FEC (Fluoroethylene carbonate, Sigma Aldrich) as an electrolyte additive was used as received. Two GF separator (diameter of 12 mm) were used as separator and were soaked with 150 μL of the electrolyte. The size of the working and counter electrodes in this case were of 10 mm diameter each. GCPL (galvanostatic charge and discharge with potential limitation) experiments in coin cell set up were conducted on a BCS-805 battery cycler from BioLogic with 5 seconds of resting period between charging and discharging cycles. GCPL experiments in three electrodes set up were performed on an MPG-2 potentiostat from BioLogic. The temperature during the GCPL experiments was maintained at 25°C. The GC cycling was performed between 2.0–4.0 V vs. Na^+/Na for Na | PW cells and between 1.0–4.0 V for graphite | PW cells. In case of three electrode cells, the potential limitation was kept only for the PW electrodes and the counter electrode potential was allowed to evolve without any potential limitation.

Full cell fabrication: The PW electrodes were used as fabricated without any prior electrochemical activation. The graphite anodes were first activated by cycling them four times with metallic sodium between 2.0 and 0.01 V and then left in a sodiated state in the fifth cycle at 0.01 V, all in constant current mode with potential limitation in respective electrolytes. No constant potential sodiation was employed. The full cells were then fabricated with the activated graphite anodes, as fabricated PW electrodes with two glass fibre separators soaked with 150 μL of the electrolyte.

Acknowledgements

S. G. P. acknowledges funding received from the Alexander von Humboldt Foundation for Postdoctoral researchers (AvH Stiftung, Germany). P. A. and G. F. thank the European Research Council (ERC) under the European Union's Horizon 2020 research and innovation programme (grant agreement no. [864698]) P. A. also acknowledges support from project TRANSITION (03XP0186B), funded by the Bundesministerium für Bildung und Forschung (BMBF). The authors thank BASF for providing high-purity sodium. Open Access funding enabled and organized by Projekt DEAL.

Conflict of Interest

The authors declare no conflict of interest.

Data Availability Statement

The data that support the findings of this study are available from the corresponding author upon reasonable request.

Keywords: electrolyte • glymes • graphite • prussian white cathodes • sodium-ion batteries

- [1] J. Qian, C. Wu, Y. Cao, Z. Ma, Y. Huang, X. Ai, H. Yang, *Adv. Energy Mater.* **2018**, *8*, 1702619.
- [2] K. Hurlbutt, S. Wheeler, I. Capone, M. Pasta, *Joule* **2018**, *2*, 1950.
- [3] W. J. Li, C. Han, G. Cheng, S. L. Chou, H. K. Liu, S. X. Dou, *Small* **2019**, *15*, 1.
- [4] T. Shibata, Y. Moritomo, *Chem. Commun.* **2014**, *50*, 12941.
- [5] W. Wang, Y. Gang, Z. Hu, Z. Yan, W. Li, Y. Li, Q. F. Gu, Z. Wang, S. L. Chou, H. K. Liu, S. X. Dou, *Nat. Commun.* **2020**, *11*, 1.
- [6] M. Pasta, R. Y. Wang, R. Ruffo, R. Qiao, H.-W. Lee, B. Shyam, M. Guo, Y. Wang, L. A. Wray, W. Yang, M. F. Toney, Y. Cui, *J. Mater. Chem. A* **2016**, *4*, 4211.
- [7] P. Adelhelm, P. Hartmann, C. L. Bender, M. Busche, C. Eufinger, J. Janek, *Beilstein J. Nanotechnol.* **2015**, *6*, 1016.
- [8] J. Zhang, D. W. Wang, W. Lv, L. Qin, S. Niu, S. Zhang, T. Cao, F. Kang, Q. H. Yang, in *Ethers Illume Sodium-Based Battery Chemistry: Uniqueness, Surprise, and Challenges*, Vol. 8, Wiley-VCH Verlag, **2018**.
- [9] N. Ortiz Vitoriano, I. Ruiz de Larramendi, R. L. Sacci, I. Lozano, C. A. Bridges, O. Arcelus, M. Enterria, J. Carrasco, T. Rojo, G. M. Veith, *Energy Storage Mater.* **2020**, *29*, 235.
- [10] L. Medenbach, P. Adelhelm, in *Electrochemical Energy Storage* (Ed.: Rüdiger-A. Eichel), **2019**, pp. 101–125.
- [11] Q. Zou, Y. Lu, *EcoMat* **2021**, *3*.
- [12] M. L. Divya, Y.-S. Lee, V. Aravindan, *ACS Energy Lett.* **2021**, *6*, 4228.
- [13] J. Park, Z.-L. Xu, K. Kang, *Front. Chem.* **2020**, *8*.
- [14] Y. Li, Y. Lu, P. Adelhelm, M. M. Titirici, Y. S. Hu, *Intercalation chemistry of graphite: Alkali metal ions and beyond*, Vol. 48, Royal Society of Chemistry, **2019**, pp. 4655–4687.
- [15] B. Jache, P. Adelhelm, *Angew. Chem. Int. Ed.* **2014**, *53*, 10169.
- [16] B. Jache, J. O. Binder, T. Abe, P. Adelhelm, *Phys. Chem. Chem. Phys.* **2016**, *18*, 14299.
- [17] K. Nobuhara, H. Nakayama, M. Nose, S. Nakanishi, H. Iba, *J. Power Sources* **2013**, *243*, 585.
- [18] M. Goktas, C. Bolli, E. J. Berg, P. Novák, K. Pollok, F. Langenhorst, M. v Roeder, O. Lenchuk, D. Mollenhauer, P. Adelhelm, *Adv. Energy Mater.* **2018**, *8*, 1.
- [19] H. Kim, K. Lim, G. Yoon, J. H. Park, K. Ku, H. D. Lim, Y. E. Sung, K. Kang, *Adv. Energy Mater.* **2017**, *7*, 1700418.
- [20] I. Escher, Y. Kravets, G. A. Ferrero, M. Goktas, P. Adelhelm, *Energy Technol.* **2021**, *9*, 2000880.
- [21] K. Westman, R. Dugas, P. Jankowski, W. Wieczorek, G. Gachot, M. Morcrette, E. Irisarri, A. Ponrouch, M. R. Palacín, J. M. Tarascon, P. Johansson, *ACS Appl. Energ. Mater.* **2018**, *1*, 2671.
- [22] H. Jia, Y. Xu, S. D. Burton, P. Gao, X. Zhang, B. E. Matthews, M. H. Engelhard, L. Zhong, M. E. Bowden, B. Xiao, K. S. Han, C. Wang, W. Xu, *ACS Appl. Mater. Interfaces* **2020**, *12*, 54893.
- [23] M. Goktas, C. Bolli, J. Buchheim, E. J. Berg, P. Novák, F. Bonilla, T. Rojo, S. Komaba, K. Kubota, P. Adelhelm, *ACS Appl. Mater. Interfaces* **2019**, *11*, 32844.
- [24] Y. Niu, Y. Yin, Y. Guo, *Small* **2019**, *15*, 1900233.
- [25] Y. You, X. L. Wu, Y. X. Yin, Y. G. Guo, *Energy Environ. Sci.* **2014**, *7*, 1643.
- [26] W. R. Brant, R. Mogensen, S. Colbin, D. O. Ojwang, S. Schmid, L. Häggström, T. Ericsson, A. Jaworski, A. J. Pell, R. Younesi, *Chem. Mater.* **2019**, *31*, 7203.
- [27] C. Q. X. Lim, Z. K. Tan, *ACS Appl. Energ. Mater.* **2021**, *4*, 6214.
- [28] W. J. Li, S. L. Chou, J. Z. Wang, Y. M. Kang, J. L. Wang, Y. Liu, Q. F. Gu, H. K. Liu, S. X. Dou, *Chem. Mater.* **2015**, *27*, 1997.
- [29] G. Leftheriotis, P. Yianoulis, in *Comprehensive Renewable Energy*, Elsevier, **2012**, pp. 313–355.
- [30] S. F. A. Kettle, E. Diana, E. M. C. Marchese, E. Boccaleri, G. Croce, T. Sheng, P. L. Stanghellini, *Eur. J. Inorg. Chem.* **2010**, *2010*, 3920.
- [31] K. R. Dunbar, R. A. Heintz, in *Progress in Inorganic Chemistry*, Volume 45, **2007**, pp. 283–391.
- [32] D. O. Ojwang, L. Häggström, T. Ericsson, J. Angström, W. R. Brant, *Dalton Trans.* **2020**, *49*, 3570.
- [33] A. Zhou, W. Cheng, W. Wang, Q. Zhao, J. Xie, W. Zhang, H. Gao, L. Xue, J. Li, in *Hexacyanoferrate-Type Prussian Blue Analogs: Principles and Advances Toward High-Performance Sodium and Potassium Ion Batteries*, Vol. 11, Wiley-VCH Verlag, **2021**.
- [34] M. J. Piernas-Muñoz, E. Castillo-Martínez, J. L. Gómez-Cámer, T. Rojo, *Electrochim. Acta* **2016**, *200*, 123.
- [35] N. Ortiz Vitoriano, I. Ruiz de Larramendi, R. L. Sacci, I. Lozano, C. A. Bridges, O. Arcelus, M. Enterria, J. Carrasco, T. Rojo, G. M. Veith, *Energy Storage Mater.* **2020**, *29*, 235.
- [36] G. Eshetu, G. A. Elia, M. Armand, M. Forsyth, S. Komaba, T. Rojo, S. Passerini, in *Electrolytes and Interphases in Sodium-Based Rechargeable Batteries: Recent Advances and Perspectives*, Vol. 10, Wiley-VCH Verlag, **2020**.
- [37] D. O. Ojwang, M. Svensson, C. Njel, R. Mogensen, A. S. Menon, T. Ericsson, L. Häggström, J. Maibach, W. R. Brant, *ACS Appl. Mater. Interfaces* **2021**, *13*, 10054.
- [38] T. D. Hatchard, M. N. Obrovac, *J. Electrochem. Soc.* **2014**, *161*, A1748.
- [39] J. Conder, C. Villevieille, *Chem. Commun.* **2019**, *55*, 1275.
- [40] K. Pfeifer, S. Arnold, J. Becherer, C. Das, J. Maibach, H. Ehrenberg, S. Soke, *ChemSusChem* **2019**, *12*, 3312.
- [41] A. P. Cohn, K. Share, R. Carter, L. Oakes, C. L. Pint, *Nano Lett.* **2016**, *16*, 543.
- [42] M. Goktas, C. Bolli, J. Buchheim, E. J. Berg, P. Novák, F. Bonilla, T. Rojo, S. Komaba, K. Kubota, P. Adelhelm, *ACS Appl. Mater. Interfaces* **2019**, *11*, 32844.
- [43] T. Palanisvam, M. Goktas, B. Anothumakkool, Y. N. Sun, R. Schmuck, L. Zhao, B. H. Han, M. Winter, P. Adelhelm, *Adv. Funct. Mater.* **2019**, *29*, 1.
- [44] M. Goktas, C. Bolli, E. J. Berg, P. Novák, K. Pollok, F. Langenhorst, M. v Roeder, O. Lenchuk, D. Mollenhauer, P. Adelhelm, *Adv. Energy Mater.* **2018**, *8*, 1702724.
- [45] T. Zhu, P. Hu, C. Cai, Z. Liu, G. Hu, Q. Kuang, L. Mai, L. Zhou, *Nano Energy* **2020**, *70*, 104548.
- [46] J. Zhang, Y. Liu, X. Zhao, L. He, H. Liu, Y. Song, S. Sun, Q. Li, X. Xing, J. Chen, *Adv. Mater.* **2020**, *32*, 1.
- [47] Z. L. Xu, G. Yoon, K. Y. Park, H. Park, O. Tamwattana, S. Joo Kim, W. M. Seong, K. Kang, *Nat. Commun.* **2019**, *10*, 1.
- [48] J. Shi, L. Ding, Y. Wan, L. Mi, L. Chen, D. Yang, Y. Hu, W. Chen, *J. Energy Chem.* **2021**, *57*, 650.
- [49] H. Li, L. Peng, Y. Zhu, D. Chen, X. Zhang, G. Yu, *Energy Environ. Sci.* **2016**, *9*, 3399.
- [50] B. Peng, Z. Sun, L. Zhao, J. Li, G. Zhang, *Energy Storage Mater.* **2021**, *35*, 620.
- [51] I. Hasa, X. Dou, D. Buchholz, Y. Shao-Horn, J. Hassoun, S. Passerini, B. Scrosati, *J. Power Sources* **2016**, *310*, 26.
- [52] Z. Zhu, F. Cheng, Z. Hu, Z. Niu, J. Chen, *J. Power Sources* **2015**, *293*, 626.
- [53] C. Q. X. Lim, Z. K. Tan, *ACS Appl. Energ. Mater.* **2021**, *4*, 6214.

Manuscript received: January 24, 2022

Revised manuscript received: February 24, 2022

Accepted manuscript online: March 15, 2022

Version of record online: April 1, 2022